Electrical Power and Energy Systems 170 (2025) 110893

Contents lists available at ScienceDirect

International Journal of Electrical Power and Energy Systems

journal homepage: www.elsevier.com/locate/ijepes

Operando monitoring and prediction of temperature in commercial sodium-ion batteries via optical fiber sensors[☆]

Yuan Wang [a,1], Yuantian Guo [b,1], Shuyan Guo [a], Guoming Ma [b], Hao Zhao [a,*]

[a] College of Engineering, Peking University, Beijing 100871, PR China
[b] State Key Laboratory of Alternate Electrical Power System with Renewable Energy Sources, North China Electric Power University, Beijing 102206, PR China

ARTICLE INFO

Keywords:
Sodium-ion battery
Layered oxides cathode
Operando monitoring
fiber Bragg grating
Battery temperature

ABSTRACT

Operando monitoring and modeling of complex thermal events inside batteries during operation is critical to understand its thermal runaway mechanism and establish early warning strategies. In this work, a compact sensing system is introduced to sodium-ion batteries based on fiber Bragg gratings. It is capable of monitoring the internal and surface temperatures during batteries operation by arranging optical fibers inside and on the surface of a commercial 18,650 battery, respectively. By applying 2 Hz square-wave current pulse on the battery, the heat transfer coefficients and the heat capacity are obtained. We observe a reproducible and stable correlation between the internal temperature and the surface temperature. Further analysis reveals a simplified thermal transfer model for predicting the internal temperature from the monitor of the surface temperature. The accuracy of the temperature estimation is within 0.5 ℃ and 2.9 ℃ when the charging/discharging conditions are varied from 1 C to 3 C. This operando monitoring and prediction approach of temperature in batteries provides in situ observation and early warning of thermal runaways of different batteries with high accuracy and low cost.

1. Introduction

Rechargeable batteries play a key role for sustainable energy storage and conversions in electric vehicles, aircraft propulsion, power plants, and other scenarios widely [1–3]. At present, the most commonly used batteries are lithium-ion batteries and sodium-ion batteries [4,5], while their security reliability and thermal management have gained increasing attentions for massive and centralized applications.

Sodium-ion batteries have emerged as important alternative to lithium-ion batteries due to its high safety and large sodium resource, even though the cycle life and energy density of sodium-ion batteries are inferior to those of lithium-ion batteries [6–9]. Due to the approximately 25–30 % smaller desolvation capacity of sodium ions compared to lithium ions [10], the activation barrier for sodium ion insertion and extraction is lower, which leads to superior low-temperature performance (even lower than −50 ℃ [11]). Also, under high-temperature conditions, carbon dioxide is a major component of released gases in sodium-ion batteries with relatively less flammable hydrocarbons resulting in a higher fire safety than that in lithium-ion batteries [12]. Therefore, sodium-ion batteries are well suited for power industrial applications. At present, polyanionic compounds are mostly used as cathode materials of sodium-ion batteries for their low preparation cost and light weight [13–15]. However, challenges such as low energy density and poor conductivity hinder its applications in high C-rate charging/discharging process. Therefore, a novel sodium-ion battery with layered oxides as cathode material is designed and developed rapidly because of its similarity to the ternary material fabrication process and its high energy density [16,17]. Complex phase transitions take place due to electrochemical reactions in such batteries and causes the poor structural stability of the layered cathode material. Therefore, it is necessary to pay special attentions to the in-situ monitoring and quantifications of key characteristics of the novel sodium-ion battery.

Temperature is an important characteristic parameter that reflects the operating status [18,19] of sodium-ion batteries. It is necessary to monitor the temperature during the charging and discharging process to reveal the chemical reactions inside the battery and achieve the early warning of thermal runaway. C. Forgez et al. [20] inserted a thermocouple into a $LiFePO_4$/graphite lithium-ion 26650 battery and successfully monitored the internal temperature. However, thermocouples are extremely susceptible to electromagnetic interference in batteries and

☆ This article is part of a special issue entitled: 'ICoPESA 2025' published in International Journal of Electrical Power and Energy Systems.

* Corresponding author.
E-mail address: h.zhao@pku.edu.cn (H. Zhao).

[1] These authors contributed to the work equally.

https://doi.org/10.1016/j.ijepes.2025.110893
Received 3 June 2025; Received in revised form 26 June 2025; Accepted 5 July 2025
Available online 10 July 2025
0142-0615/© 2025 The Authors. Published by Elsevier Ltd. This is an open access article under the CC BY-NC-ND license (http://creativecommons.org/licenses/by-nc-nd/4.0/).

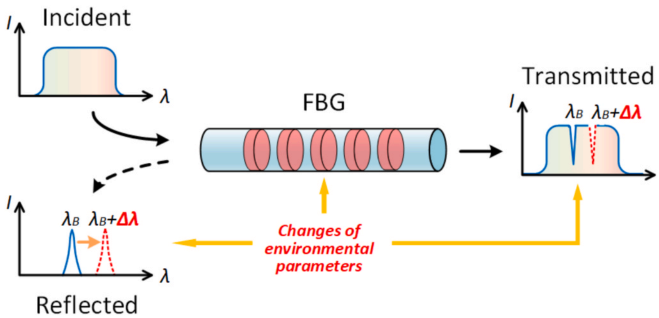

Fig. 1. Principle of fiber Bragg grating temperature sensing.

are not suitable for battery temperature quantifications with a high temporal-spatial resolution. Meanwhile, the inserted thermocouple is very likely to affect battery performance due to its geometry size. Therefore, new operando techniques for temperature monitoring need to be developed.

Compared with traditional electronic temperature sensors, optical fiber sensors have the advantages of excellent electrical insulation, anti-electromagnetic interference, compact structure, fast response time, and high sensitivity [21–25]. J. Pinto et al. firstly integrated optical fiber sensor in lithium batteries for real-time temperature monitor [26]. M. Nascimento et al. pasted fiber Bragg grating (FBG) sensors on a battery surface and achieved the simultaneous measurements of temperature and stress [27]. Recently, Huang group and Guo and Mei group [13,14,18,28] inserted FBG sensors into lithium-ion 18,650 batteries to monitor the internal temperature changes during the charging/discharging cycles, respectively. These studies have demonstrated the feasibility of using optical fiber sensors for lithium-ion battery internal temperature monitoring, providing a sensing solution for monitoring the operational characteristics of the sodium-ion battery. However, in the aforementioned research, most studies were conducted within temperature chambers, which cannot accurately reflect the temperature variations under actual operating conditions. Also, in practical thermal managements of batteries, it is challenging to insert optical fiber sensors to each battery for temperature monitoring with high cost and complexity. There is a lack of real-time, effective, and low-cost techniques to monitor and predict the internal temperatures of sodium-ion batteries through certain external characteristic parameters. One promising solution is to develop a non-destructive internal temperature predictive model based on the measured internal and surface temperatures of the same type of battery.

In order to understand the thermal processes during the charging/discharging cycles of the novel sodium-ion battery and build the non-destructive temperature prediction model, we implant the FBG temperature sensors inside and on surface of 18,650 cylindrical batteries. The internal temperature rise during charging/discharging cycles at different C-rates of different types of sodium-ion batteries are quantified and analyzed. Simultaneously, the surface temperature of the battery and the ambient temperature are also monitored. Furthermore, a simplified thermal model between surface and internal temperatures of batteries is proposed to predict thermal events of batteries with high accuracy.

2. Experimental setup and method

2.1. Principle of fiber Bragg grating temperature sensing

A fiber Bragg grating (FBG) is an optical component in which a Bragg reflector is inscribed in an optical fiber with a uniform diameter of 125 μm. For a broadband source, only the light with a specific wavelength (the Bragg wavelength, λ_B) is reflected by FBG, and all others are transmitted. Fig. 1 shows the schematic and the principle of the FBG sensor. The basic measurement is based on monitoring the shifts in reflected wavelength as local temperature (ΔT) and strain changes ($\Delta\varepsilon$) around the FBG sensor. The relative shift in the Bragg wavelength $\Delta\lambda_B / \lambda_B$ can be approximately given as [29]

$$\frac{\Delta\lambda_B}{\lambda_B} = (\alpha_f + \xi)\Delta T + (1 - p_e)\Delta\varepsilon \quad (1)$$

where ξ is the thermo-optic coefficient, α_f is the thermal expansion coefficient of the optical fiber, p_e is the effective photo-elastic constant.

If the applied strain remains constant, the shifts in reflected wavelength are only determined by the temperature variation. Thus, the FBGs can be selected as an operando sensing probe for temperature measurements.

To identify the FBG's temperature response, a FBG was placed into a water bath cauldron, and the temperature was varied from 25 ℃ to 80 ℃. The shifts in reflected wavelength of the FBG is shown in Fig. 2(a). The results show that there is a good linear relationship between temperature change and reflected wavelength shift. The temperature sensitivity is about 10.6 pm/℃ ($R^2 = 0.998$). Moreover, there will be pressure fluctuation during the charge/discharge in the battery. To verify the reliability of the FBG sensor, the pressure response within 0.2 MPa was tested. It can be seen from Fig. 2(b), pressure fluctuations have

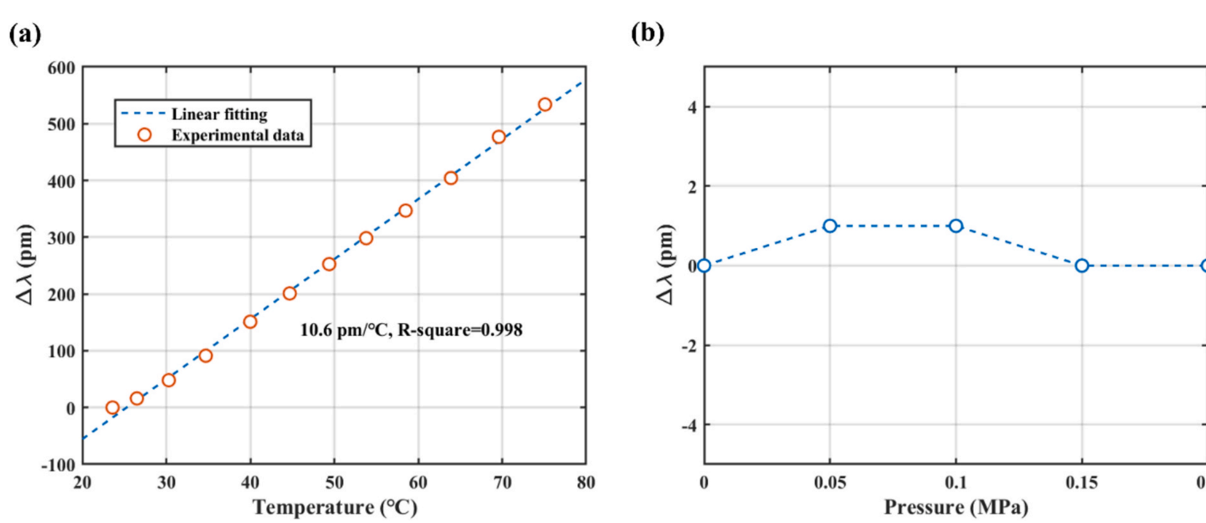

Fig. 2. The wavelength responses to temperature and pressure of the FBG sensor. (a) Wavelength responses to temperature over the range of 25 to 80 ℃. (b) Wavelength responses to pressure over the range of 0 to 0.2 MPa.

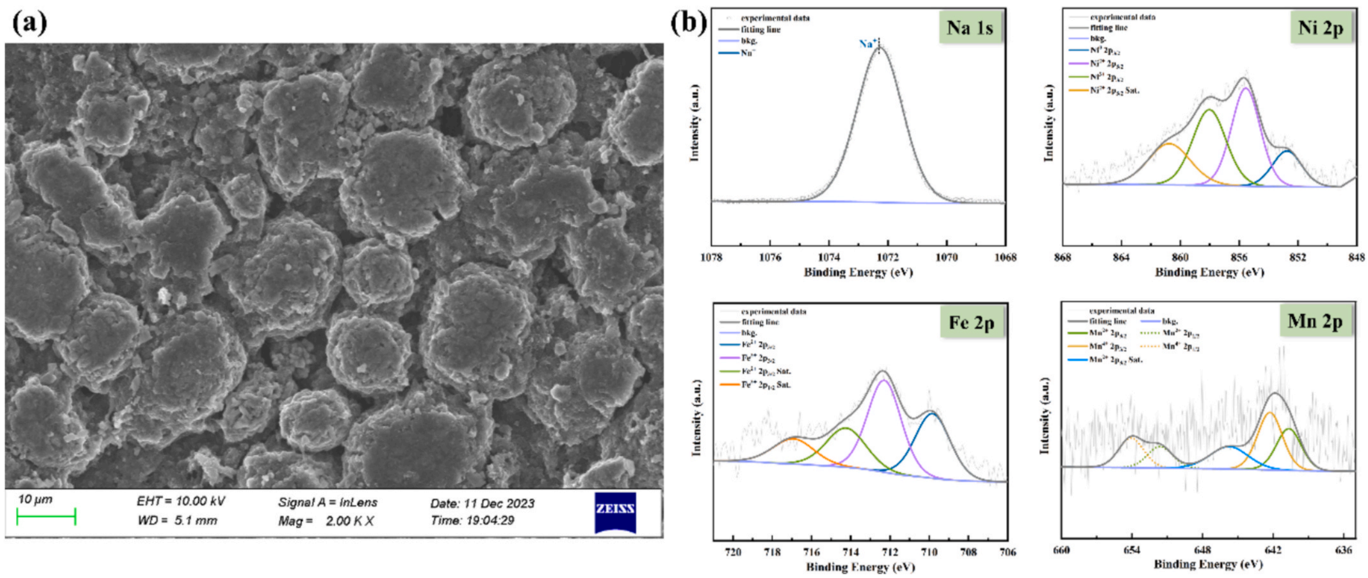

Fig. 3. (a) SEM image of the Ni-Fe-Mn-based cathode material, (b) XPS image of the cathode material disassembled from a fresh battery.

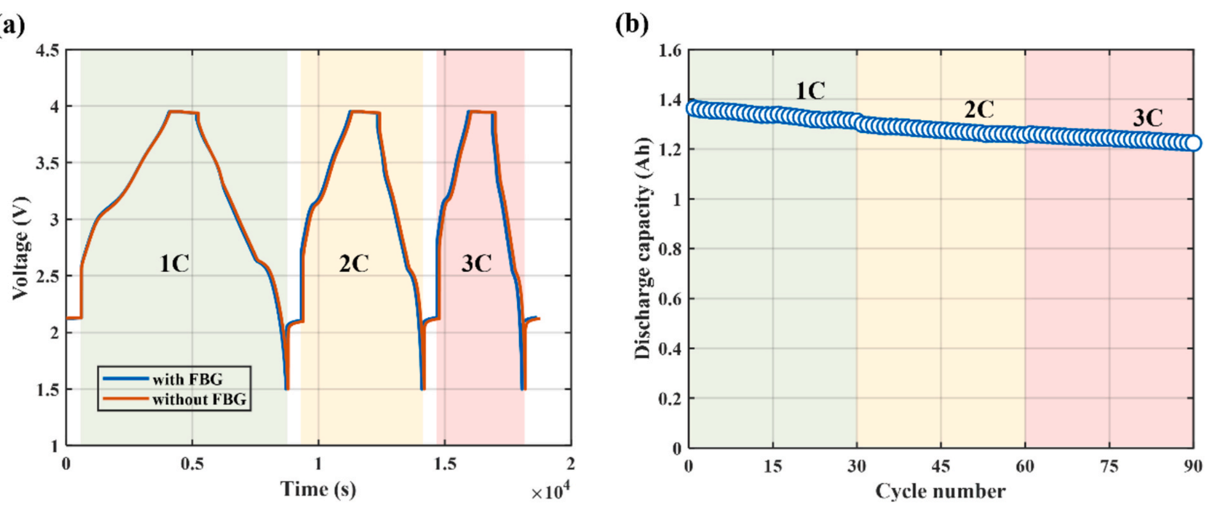

Fig. 4. The performance of battery is unaffected by FBG sensors. (a) Comparison of battery voltage before and after FBG implantation when cycled at 1 C, 2 C and 3 C. (b) Battery performance remaining unaffected after FBG implantation by cycling at different C-rates for 90 cycles.

little effect on the response of the FBG sensor, which represents that the influence of pressure change in batteries can be ignored.

2.2. Integration of FBG sensor into the sodium-ion 18650 battery

In this paper, a novel sodium-ion 18650 battery ([Xuexiong, NaFR18/065CY-1.3]) using layered oxides as cathode materials is focused on. In addressing the phase transition issue during the deintercalation process of layered oxides, the battery employs a Ni-Fe-Mn-based cathode material. Simultaneously, Mg^{2+} is doped to improve the chemical stability, and enhance the conductivity. In addition, cobalt phosphate ($Co_3(PO_4)_2$) is also introduced to stabilize the material structure and reduce cathode material corrosion, improving safety. The battery is based on sodium-ion $Na_a(Ni_xFe_yMn_{1-x-y})_{2-a}O_2$/hard carbon chemistry, and the rated capacity is 1300 mAh. Using this type of layered oxide as a cathode material can help improve the energy density and safety of batteries, which contributes to improving the performance and expanding the application range of sodium-ion batteries. The scanning electron microscope (SEM) image and the X-ray photoelectron spectroscopy (XPS) of the cathode material disassembled from a fresh sodium-ion battery are shown in Fig. 3.

In order to implant the FBG sensor into the battery, a 1 mm hole was drilled at the central position of the negative pole of the battery in a glove box. For reducing the risk during drilling, the fresh battery was first discharged to 0 % SOC. The FBG sensor was inserted into the battery through the central hole and was parallel to the axis of the battery. In this way, the FBG sensor is almost not affected by any undesirable stress. Therefore, the shifts in reflected wavelength are considered to be only caused by the changes in environmental temperature. After placement, the insertion point was sealed with epoxy resin (chemically stable and thermally resistant) to prevent air or moisture ingress. The seal was cured at room temperature for 48 h.

To verify the impact of implanted FBG sensor on battery performance, the sodium-ion 18650 batteries with/without FBG sensor were operated charge and discharge cycles at different C-rates of 1 C, 2 C and 3 C. The batteries were cycled through 30 charging/discharging cycles at each C-rates. During the verification, a 10 min rest was set between charge and discharge to allow the battery temperature to decrease. Furthermore, to simulate the normal operating conditions of the batteries, the batteries were placed in the atmospheric Environment without

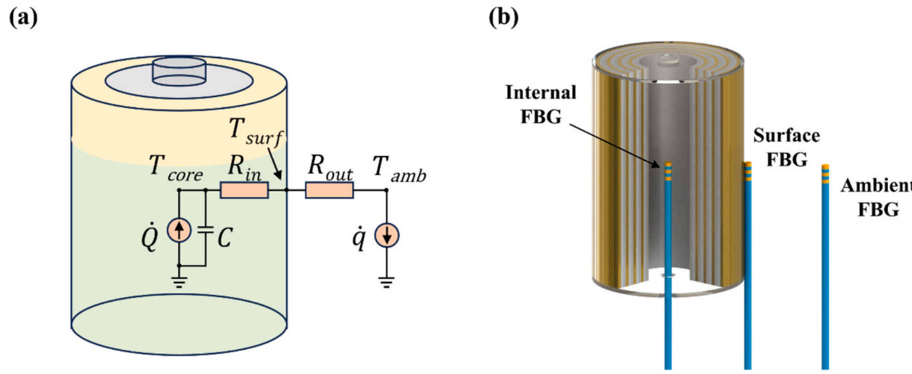

Fig. 5. (a) Simplified thermal model of sodium-ion 18650 battery. (b) Schematic diagram of FBG sensors arrangement.

temperature control. Fig. 4(a) and (b) show that the cycle curves before and after the FBG sensor implantation have good consistency, and the capacity of the battery with FBG sensor implantation only decays by 1.75 % after 90 cycles at different C-rates. The results demonstrated that the introduction of FBG did not have a negative impact on battery performance.

3. Determination of thermal model

3.1. Establish of the thermal model

For 18650 batteries, the heat generated during the charging/discharging cycle spreads to the battery surface and then to the external environment. When the battery internal temperature (T_{core}), battery surface temperature (T_{surf}) and ambient temperature (T_{amb}) are obtained simultaneously, a simplified zero-dimensional thermal-circuit model can be established, as shown in Fig. 5 (a). In this simplified model, capacitance represents heat capacity and resistances represent the

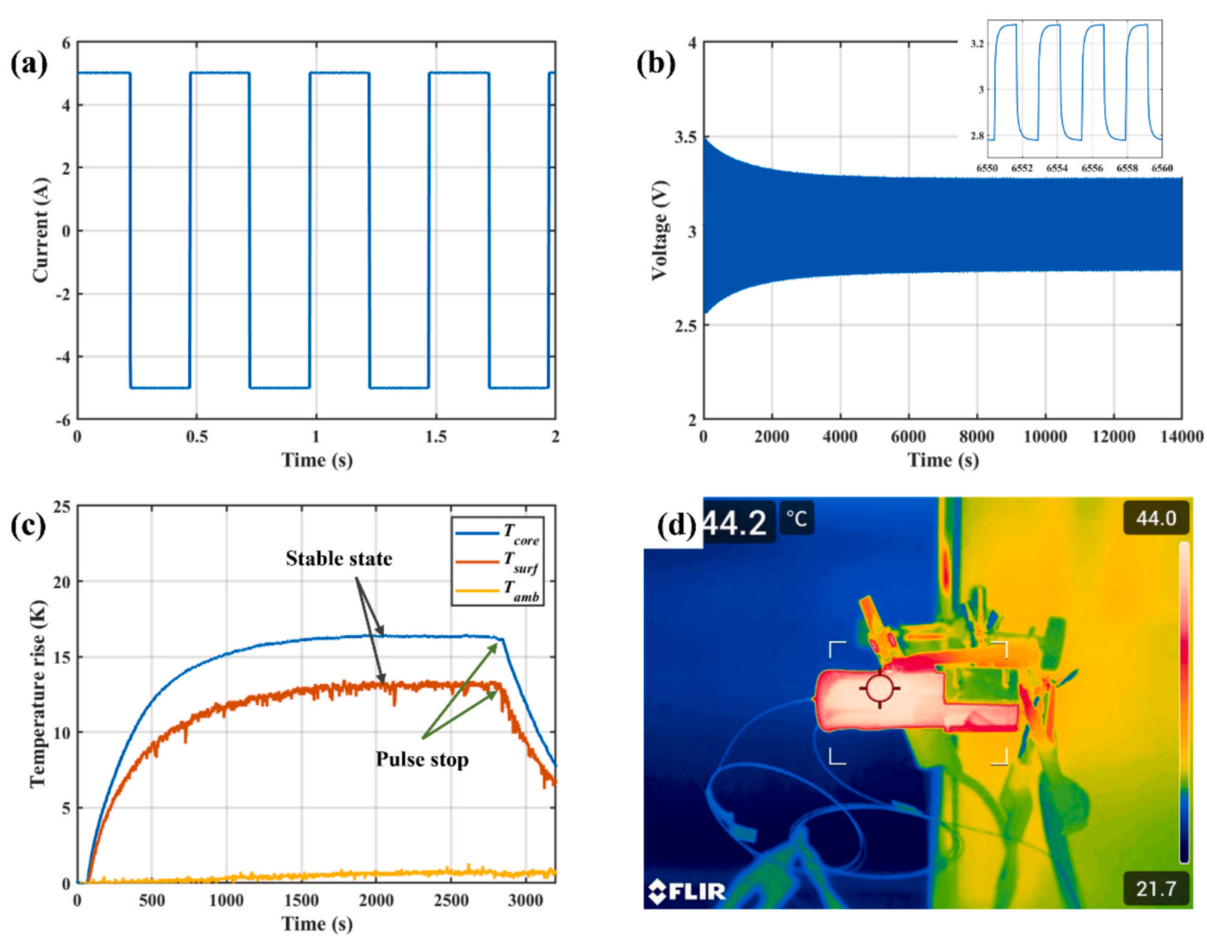

Fig. 6. (a) The square-wave current pulse of 2 Hz applied in the battery. (b) The battery voltage changes upon applying symmetric and periodic square-wave current pulse. (c) Temperature changes at different locations during the test. (d) Infrared image of the battery temperature under the steady state (± 5 A).

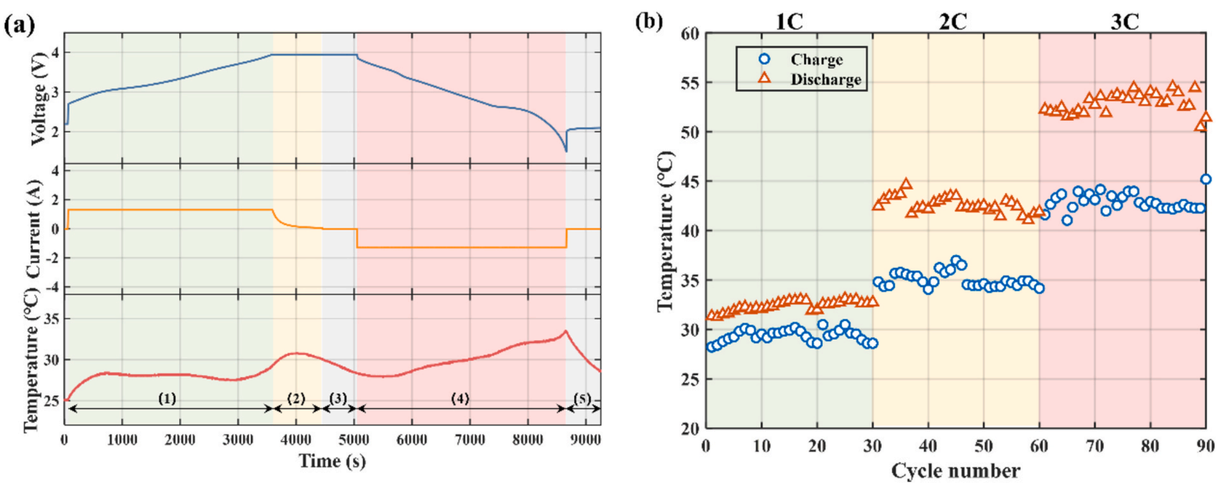

Fig. 7. (a) The relationship among voltage, current and internal temperature monitored by FBG sensor at 1 C cycling, (1) CC, (2) CV, (3) and (5) resting, (4) CCD. (b) The maximum temperature during different charging/discharging cycles and different C-rates.

reciprocal of heat transfer coefficients.

The heat generation rate of the battery ($\dot{Q}$) can be expressed as [13,20]

$$\dot{Q} = C\frac{\partial T_{core}}{\partial t} + \dot{q} \tag{2}$$

where C represents heat capacity, t stands for time, and $\dot{q}$ is the heat flow rate from the battery to the ambient environment. $\dot{q}$ is given as

$$\dot{q} = \frac{T_{core} - T_{surf}}{R_{in}} = \frac{T_{surf} - T_{amb}}{R_{out}} \tag{3}$$

In Eq. (3), R_{in} and R_{out} respectively represent the equivalent thermal resistance between the inside of the battery and the battery surface and the equivalent thermal resistance between the battery surface and the ambient environment.

According to the expression derived by K.E. Thomas and partial simplification, $\dot{Q}$ can also be written into [20,30]

$$\dot{Q} = I(V - U) + IT_{core}\frac{\partial U}{\partial T_{core}} \tag{4}$$

with I being the current, V being the battery voltage, U being the battery thermodynamic equilibrium potential.

3.2. Determination of parameters

According to the Eq. (2) to Eq. (4), in order to grasp the thermal process of the battery, it is necessary to obtain the parameters (C, R_{in}, R_{out}) under the known heat generation rate ($\dot{Q}$) and temperatures (T_{core}, T_{surf}, T_{amb}). If a symmetric and periodic square-wave current pulse is applied to the battery, the SOC remains constant because the net charge transfer over each full cycle is zero. This results from equal and opposite charging and discharging currents in both magnitude and duration. Since SOC is defined as the ratio of remaining charge to total capacity, it stays unchanged under this condition, provided there are no significant side reactions (e.g., self-discharge or leakage) and the battery operates within its reversible range. According to the Nernst equation [21], the thermodynamic equilibrium potential U can be regarded as a certain value. That is, within a single current pulse period, T_{core} can be seen as constant. Thus, the second term in Eq. (4) can be ignored, and the heat generation rate ($\dot{Q}$) can be calculated. When heat production and heat dissipation reach a steady state, $\dot{Q}$ equals to $\dot{q}$. R_{in} and R_{out} can be obtained based on Eq. (3), and then C can be calculated by Eq. (2). Finally, the parameters for the thermal model of sodium-ion 18650 battery are grasped.

Three FBG sensors was placed inside the battery, on the battery surface and in the ambient environment to monitor temperature changes during charging/discharging, as shown in Fig. 5 (b). In order to raise the temperature while remaining the SOC constant, a square-wave current pulse with 2 Hz frequency and ±5 A amplitude (as shown in Fig. 6 (a)) was applied in the battery to generate a known heat using a bipolar power supply (BP4620, NF, Japan). By choosing a 2 Hz frequency, each half-cycle lasts only 0.25 s, which is much shorter than the battery's thermal time constant [20]. Therefore, heat accumulates over multiple cycles without allowing significant thermal relaxation between pulses, leading to a gradual and measurable temperature increase representative of the battery's heating characteristics.

The voltage between the positive and negative electrodes of the battery is shown in Fig. 6 (b). During this process, the battery temperature gradually increased and finally entered a stable state after 1600 s, as shown in Fig. 6 (c). The maximum temperature rise was about 16.5 K for the battery internal temperature. The infrared imaging of battery temperature under the steady state is shown in Fig. 6 (d).

According to the Eq. (2) to Eq. (4), for the sodium-ion 18650 battery using layered oxides as cathode materials, the heat generation rate $\dot{Q}$ is about 1.22 W at the stable state, and the calculated results of R_{in}, R_{out}, and C are 2.99 K/W, 10.80 K/W, and 21.58 J/K, respectively. These parameters are representative of other identical batteries of the same type and specification, assuming basic consistent manufacturing quality and operating conditions.

4. Results and discussion

4.1. Internal temperature changes at different C-rates

In order to evaluate the temperature changes during the charging/discharging cycles of the novel sodium-ion battery, the battery got charged and discharged at different C-rates (1 C, 2 C, and 3 C) in this paper. To display the changes in battery temperature under normal operating conditions, the environmental temperature was not controlled. Meanwhile, the FBG sensors were used to monitor the internal temperature, surface temperature and ambient temperature. The whole cycle consisted of steps as constant current (CC) charging, constant voltage (CV) charging, resting, constant current discharging (CCD) and resting. Taking 1 C as an example, the variations in voltage, current, and internal temperature are shown in Fig. 7.

It can be seen from Fig. 7 and the traditional lithium-ion battery charging/discharging curve that, during CC charging and CCD, the voltage changes sharper than that of lithium-ion batteries, so the

Table 1
Performance comparison of different types of rechargeable batteries.

Type of battery	Cathode material	C-rate	Capacity	Maximum temperature rise	Ref.
Li-ion, 26650	$LiFePO_4$	6 C	–	16.0 K	[20]
Li-ion, 18650	$LiFePO_4$	1 C	1.653 Ah	5.2 K	[28]
Na-ion, 18650	$Na_3V_2(PO_4)_2F_3$	1 C	0.800 Ah	6.0 K	[12]
Na-ion, 18650	$Na_a(Ni_xFe_yMn_{1-x-y})_{2-a}O_2$	1 C	1.300 Ah	8.2 K	This paper

temperature rise is also more obvious. In addition, during a charging/discharging cycle, the highest peak of temperature rise occurs at the end of discharging, which indicates that special attention needs to be paid to the temperature rise during discharge. And the maximum temperature rises at different C-rates are about 8.2 K for 1 C, 19.1 K for 2 C, and 29.5 K for 3 C. Moreover, as the C-rate increased, the internal temperature of the battery increased significantly.

A mini performance comparison of different types of rechargeable batteries is shown in Table 1. Compared with the $Na_3V_2(PO_4)_2F_3$/hard carbon battery, the novel sodium-ion battery used in this paper has a higher capacity and a relatively weak temperature rise, which shows good application prospects. Compared with lithium-ion batteries, the novel sodium-ion battery used in this paper has a lower capacity, but generates more heat during the charging/discharging cycles, resulting in a more dramatic temperature rise.

4.2. Prediction under different current

By the simplified zero-dimensional thermal-circuit model, the internal temperature of the battery can be predicted by the surface temperature and ambient temperature, as

$$T_{core} = \frac{R_{out} + R_{in}}{R_{out}} T_{surf} - \frac{R_{in}}{R_{out}} T_{amb} \tag{5}$$

In this section, the battery was cycled at different C-rates for 90 cycles (1 C, 2 C and 3 C, and cycled 30 times at each C-rates), using FBG sensors to monitor the surface temperature and ambient temperature. Combined with the model parameters mentioned in *Section 3.2*, the internal temperature was predicted and compared with the actual measurement results. The results are shown in Fig. 8.

It can be seen that the predicted temperature was in good agreement with the measured temperature. And the maximum errors were about 0.5 ℃ for 1 C, 1.0 ℃ for 2 C, and 2.9 ℃ for 3 C. Therefore, with the measured battery surface temperature and Eq. (5), the internal temperature can be obtained. It provides a real-time, effective, accurate, and low-cost technique for monitoring and predicting battery internal temperatures. At the same time, the FBG temperature sensor has a compact structure with capability of strong anti-electromagnetic interference and excellent reliability in harsh environments. It is very suitable for monitoring batteries in electric vehicles, energy storage power stations, and other fields.

5. Conclusion

This paper employed a promising FBG temperature sensor to predict the internal temperature by simultaneously monitoring the surface temperature and ambient temperature during the charging/discharging cycles of a novel sodium-ion battery using layered oxides as cathode material. An FBG sensor was implanted into the battery to operando monitoring the internal temperature, and it was verified that the implantation of FBG sensor had almost no impact on battery performance. The study found that the maximum temperature rise occurs at the end of discharging stage during a complete charging/discharging cycle. Therefore, the battery management system should particularly focus on monitoring temperature changes during discharging stage. And the maximum internal temperature rise increases significantly with the increase of C-rate, which is about 8.2 K for 1C, 24.1 K for 2C, and 33.9 K for 3C. Moreover, a stable correlation between the internal temperature and both the surface temperature and ambient temperature is found. By applying square-wave current pulse on the battery, the thermal parameters of the battery were figured out, and a simplified zero-dimensional thermal-circuit model for the battery was proposed in

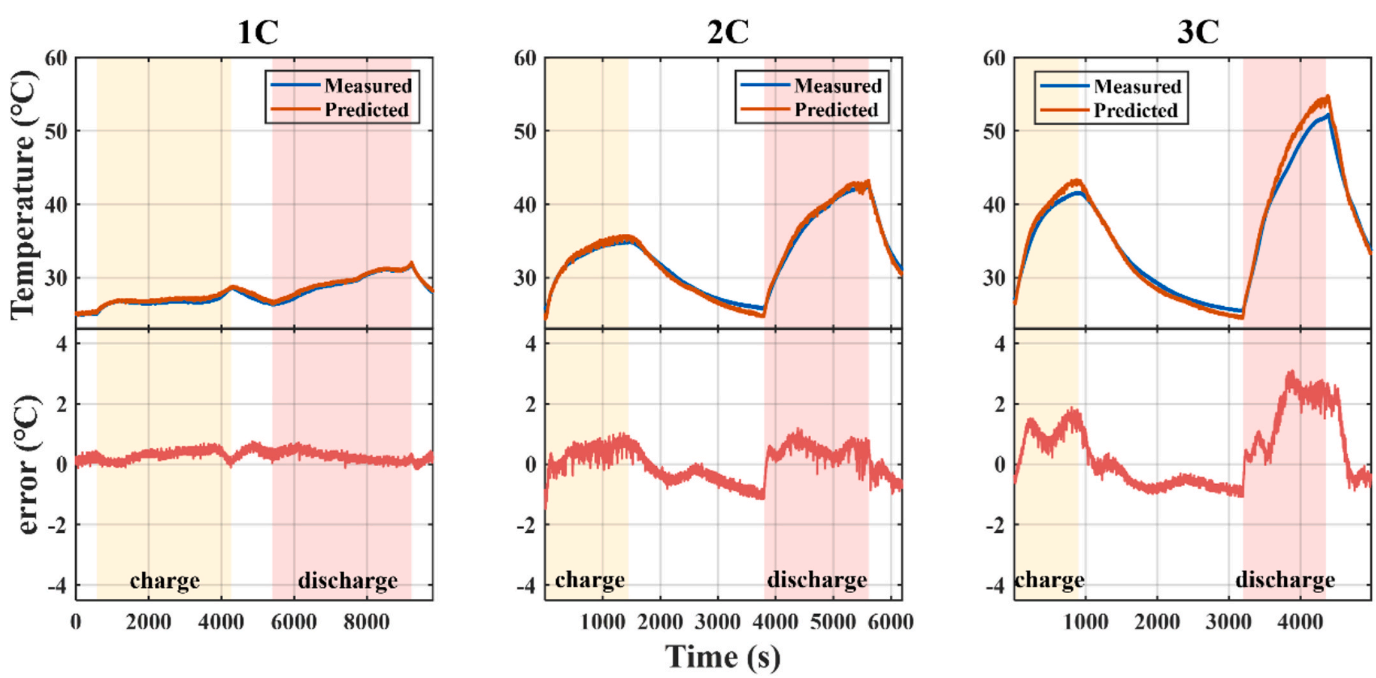

Fig. 8. Measured and predicted values of battery internal temperature at 1 C, 2 C and 3 C cycling, taken from the long-term cycles. The yellow, red and white parts are the charging stage, discharging stage and resting stage respectively. (For interpretation of the references to colour in this figure legend, the reader is referred to the web version of this article.)

turn. By using the proposed model along with the surface temperature obtained from the FBG sensor attached to the battery and the ambient temperature obtained from the FBG sensor placed near the battery, the internal temperature could be accurately predicted with uncertainties of 0.5 ℃ for 1 C, 1.0 ℃ for 2 C, and 2.9 ℃ for 3 C. Therefore, the internal temperature of the sodium-ion battery (pack) can be grasped by monitoring the surface temperature and ambient temperature. This will help to understand the thermal and chemical processes during charge and discharge of the sodium-ion batteries, and provide practical and low-cost solutions for high-precision and real-time monitoring of battery temperature in real applications such as electrical vehicles and energy storage devices.

CRediT authorship contribution statement

Yuan Wang: Writing – original draft, Visualization, Methodology, Investigation, Funding acquisition, Formal analysis, Data curation, Conceptualization. **Yuantian Guo:** Writing – review & editing, Visualization, Software, Investigation, Formal analysis, Data curation. **Shuyan Guo:** Writing – review & editing, Methodology, Formal analysis. **Guoming Ma:** Writing – review & editing, Supervision, Project administration, Methodology. **Hao Zhao:** Writing – review & editing, Project administration, Methodology, Funding acquisition.

Declaration of competing interest

The authors declare that they have no known competing financial interests or personal relationships that could have appeared to influence the work reported in this paper.

Acknowledgement

The work was funded by the National Key Research and Development Program (2023YFE0120900), the State Key Laboratory of Alternate Electrical Power System with Renewable Energy Sources (LAPS23002), the Nationally Funded Postdoctoral Researcher Program (GZC20230045). The authors are truly thankful to senior engineer Jin ZHANG at Institute of Electrical Engineering of Chinese Academy of Sciences for his technical supports of measurements under current pulses.

Data availability

No data was used for the research described in the article.

References

[1] Hannan MA, Wali SB, Ker PJ, Rahman MSA, Mansor M, Ramachandaramurthy VK, et al. Battery energy-storage system: a review of technologies, optimization objectives, constraints, approaches, and outstanding issues. J Energy Storage 2021;42:103023. https://doi.org/10.1016/j.est.2021.103023.
[2] Yang Y, Bremner S, Menictas C, Kay M. Battery energy storage system size determination in renewable energy systems: a review. Renew Sust Energ Rev 2018;91:109–25. https://doi.org/10.1016/j.rser.2018.03.047.
[3] Clarke M, Alonso JJ. Lithium–ion battery modeling for aerospace applications. J Aircraft 2021;58:1323–35. https://doi.org/10.2514/1.C036209.
[4] Han X, Lu L, Zheng Y, Feng X, Li Z, Li J, Ouyang M. A review on the key issues of the lithium ion battery degradation among the whole life cycle. eTransportation 2019;1:100005. doi: 10.1016/j.etran.2019.100005.
[5] Khan FMNU, Rasul MG, Sayem ASM, Mandal NK. Design and optimization of lithium-ion battery as an efficient energy storage device for electric vehicles: a comprehensive review. J Energy Storage 2023;71:108033. https://doi.org/10.1016/j.est.2023.108033.
[6] Slater MD, Kim D, Lee E, Johnson CS. Sodium-ion batteries. Adv. Funct. Mater. 2013;23:947–58. https://doi.org/10.1002/adfm.201200691.
[7] Yabuuchi N, Kubota K, Dahbi M, Komaba S. Research development on sodium-ion batteries. Chem. Rev. 2014;114:11636–82. https://doi.org/10.1021/cr500192f.
[8] Vaalma C, Buchholz D, Weil M, Passerini S. A cost and resource analysis of sodium-ion batteries. Nat. Rev. Mater. 2018;3:1–11. https://doi.org/10.1038/natrevmats.2018.13.
[9] Li Q, Yu X, Li H. Batteries: From China's 13th to 14th Five-Year Plan, eTransportation 14 (2022) 100201. doi: 10.1016/j.etran.2022.100201.
[10] Nayak PK, Yang L, Brehm W, Adelhelm P. From lithium-ion to sodium-ion batteries: advantages, challenges, and surprises. Angew Chem Int Edit 2018;57:102–20. https://doi.org/10.1002/anie.201703772.
[11] Abraham KM. How comparable are sodium-ion batteries to lithium-ion counterparts? ACS Energy Lett. 2020;5:3544–7. https://doi.org/10.1021/acsenergylett.0c02181.
[12] Huang J, Albero Blanquer L, Bonefacino J, Logan ER, Alves Dalla Corte D, Delacourt C, Gallant BM, Boles ST, Dahn JR, Tam H-Y, Tarascon J-M. Operando decoding of chemical and thermal events in commercial Na(Li)-ion cells via optical sensors. Nat Energy 2020;5:674–683. doi: 10.1038/s41560-020-0665-y.
[13] Huang J, Delacourt C, Desai P, Gervillié-Mouravieff C, Blanquer LA, Tan R, et al. Unravelling thermal and enthalpy evolutions of commercial sodium-ion cells upon cycling ageing via fiber optic sensors. J Electrochem Soc 2023;170:090510. https://doi.org/10.1149/1945-7111/acf625.
[14] Xiao L, Ji F, Zhang J, Chen X, Fang Y. Doping regulation in polyanionic compounds for advanced sodium-ion batteries. Small 2023;19:2205732. https://doi.org/10.1002/smll.202205732.
[15] Lv Z, Ling M, Yue M, Li X, Song M, Zheng Q, et al. Vanadium-based polyanionic compounds as cathode materials for sodium-ion batteries: toward high-energy and high-power applications. J Energy Chem 2021;55:361–90. https://doi.org/10.1016/j.jechem.2020.07.008.
[16] Wang P-F, You Y, Yin Y-X, Guo Y-G. Layered oxide cathodes for sodium-ion batteries: phase transition, air stability, and performance. Adv Energy Mater 2018;8:1701912. https://doi.org/10.1002/aenm.201701912.
[17] Zhao C, Wang Q, Yao Z, Wang J, Sánchez-Lengeling B, Ding F, et al. Rational design of layered oxide materials for sodium-ion batteries. Science 2020;370:708–11. https://doi.org/10.1126/science.aay9972.
[18] Mei W, Liu Z, Wang C, Wu C, Liu Y, Liu P, et al. Operando monitoring of thermal runaway in commercial lithium-ion cells via advanced lab-on-fiber technologies. Nat Commun 2023;14:5251. https://doi.org/10.1038/s41467-023-40995-3.
[19] Cen J, Jiang F. Li-ion power battery temperature control by a battery thermal management and vehicle cabin air conditioning integrated system. Energy Sustain Dev 2020;57:141–8. https://doi.org/10.1016/j.esd.2020.06.004.
[20] Forgez C, Vinh Do D, Friedrich G, Morcrette M, Delacourt C. Thermal modeling of a cylindrical LiFePO4/graphite lithium-ion battery. J Power Sources 2010;195:2961–8. https://doi.org/10.1016/j.jpowsour.2009.10.105.
[21] Liu L, Zhu J, Zheng L. An effective method for estimating state of charge of lithium-ion batteries based on an electrochemical model and Nernst equation. IEEE Access 2020;8:211738–49. https://doi.org/10.1109/ACCESS.2020.3039783.
[22] Huang J, Boles ST, Tarascon J-M. Sensing as the key to battery lifetime and sustainability. Nat Sustain 2022;5:194–204. https://doi.org/10.1038/s41893-022-00859-y.
[23] Han G, Yan J, Guo Z, Greenwood D, Marco J, Yu Y. A review on various optical fibre sensing methods for batteries. Renew Sust Energ Rev 2021;150:111514. https://doi.org/10.1016/j.rser.2021.111514.
[24] Wang Y, Ma G, Zheng D, Qin W, Jiang J, Zhou H, et al. Transformer oil-dissolved acetylene detection with photonic crystal fiber loop ringdown spectroscopy. Sens Actuat B Chem 2021;346:130590. https://doi.org/10.1016/j.snb.2021.130590.
[25] Tan K, Li W, Lin Z, Han X, Dai X, Li S, et al. Operando monitoring of internal gas pressure in commercial lithium-ion batteries via a MEMS-assisted fiber-optic interferometer. J Power Sources 2023;580:233471. https://doi.org/10.1016/j.jpowsour.2023.233471.
[26] Yang G, Leitão C, Li Y, Pinto J, Jiang X. Real-time temperature measurement with fiber Bragg sensors in lithium batteries for safety usage. Measurement 2013;46:3166–72. https://doi.org/10.1016/j.measurement.2013.05.027.
[27] Matuck L, Pinto JL, Marques C, Nascimento M. Simultaneous strain and temperature discrimination in 18650 Li-ion batteries using polarization-maintaining Fiber Bragg gratings. Batteries 2022;8:233. https://doi.org/10.3390/batteries8110233.
[28] Liu Y, Liu Z, Mei W, Han X, Liu P, Wang C, et al. Operando monitoring Lithium-ion battery temperature via implanting femtosecond-laser-inscribed optical fiber sensors. Measurement 2022;203:111961. https://doi.org/10.1016/j.measurement.2022.111961.
[29] Ma G, Wang Y, Qin W, Zhou H, Yan C, Jiang J, et al. Optical sensors for power transformer monitoring: a review. High Volt 2021;6:367–86. https://doi.org/10.1049/hve2.12021.
[30] Thomas KE, Newman J. Thermal modeling of porous insertion electrodes. J. Electrochem. Soc. 2003;150:A176. https://doi.org/10.1149/1.1531194.